44th AIAA Aerospace Sciences Meeting and Exhibit
9 - 12 January 2006, Reno, Nevada

AIAA 2006-156

Level-Set Flamelet/Large-Eddy Simulation of a Premixed Augmentor Flame Holder

Cosmin Safta,[*] Kehinde Alabi,[†] Foluso Ladeinde,[‡] and Xiaodan Cai[§]
Thaerocomp Technical Corporation, P.O. Box 1527, Stony Brook, NY 11790-0609

Barry Kiel[**] and Balu Sekar[††]
Air Force Research Laboratory/PRTC,Wright-Patterson Air Force Base, OH 45433

The objective of the current study is to combine a high-fidelity large eddy simulation (LES) flow solver with a level-set flamelet algorithm for the prediction of premixed turbulent combustion. The same level of high accuracy is implemented for simulation at all speeds. The goal of this work is to accurately predict the unsteady turbulence-flame interaction for realistic industrial combustors with complex geometries. The numerical issues related to the numerical implementation of the LES equations, flamelet model and level-set algorithm are presented in detail. The accuracy of the numerical implementation is verified through comparisons with experimental data for an augmentor flame holder and a turbulent Bunsen burner flame.

Nomenclature

a,b = right hand side parameter for the COMPACT scheme
c_p = specific heat at constant pressure
c_{rm} = coefficients of a Lagrange interpolation (for the WENO scheme)
D = nozzle diameter
D_p = pilot flame diameter
E = specific total energy
F, G, H = vector of convective fluxes in the physical x, y, and z directions, respectively
G = level-set function
h = specific enthalpy
F_v, G_v, H_v = vector of viscous fluxes in the physical x, y, and z directions, respectively
i,j = spatial scheme indices
J = Jacobian of the transformation between the physical and the curvilinear coordinate system
K = stretch rate
k = turbulent kinetic energy
l_F, $l_{F,t}$ = laminar and turbulent flame thickness
M = Mach number
$P(.)$ = probability density function
Pr = Prandtl number
p = thermodynamic pressure
Q = vector of conserved variables
Q_T^0 = chemical source term
q_i = component of the heat flux vector
Re = Reynolds number

---

[*] Research Engineer, AIAA Member.
[†] Research Engineer, AIAA Member.
[‡] Director of Research, AIAA Life Member and Associate Fellow.
[§] Senior Research Engineer, AIAA Member.
[**] Augmentor Program Manager, AIAA Member.
[††] Aerospace Engineer, AIAA Associate Fellow.

$\widetilde{R}_{Roe}$ = right eigenvectors matrix of $\partial\hat{F} / \partial Q$ based on a Roe-averaged state at midpoint locations
S = source term in the flow conservation equations
S_L = laminar flame velocity
S_T = laminar flame velocity
SGS = sub-grid scale
St = Strouhal number
T = temperature
t = time
u_i = velocity components
u' = velocity fluctuations
W = flame holder width
x,y,z = physical coordinate system
Y_k = mass fraction of species k

α = left-hand side parameter for the COMPACT scheme; spectral radius used in the WENO scheme
α_f = filter parameter for the compact scheme
γ = ratio of specific heats
φ = parameter for the Beam-Warming time marching scheme
κ = flame curvature
Φ = fuel-to-oxidizer equivalence ratio
ϕ = generic variable
$\nu,\ \nu_t$ = laminar and turbulent viscosities
ρ = density
ξ,η,ζ = curvilinear coordinate system
ξ_i = transformation metrices between the curvilinear and physical coordinate system
Δ = filter width
Δt = time step size
$\Delta x,\ \Delta y$ = grid size
τ_{ij} = component of the viscous stress tensor
ω = vorticity
ω_r , $\widetilde{\omega}_r$ = normalized weights for the WENO scheme
ω_k = reaction rate of species k

I. Introduction

Modern aircraft engines and gas turbine combustors are required to reduce NOx emissions for environmental reasons. While a number of approaches have been investigated for lowering pollutant emissions, lean-premixed combustion (LPM) is considered an effective and competitive means to achieve this goal.[6] As the equivalence ratio in such combustors is reduced, the adiabatic flame temperature drops as well, leading to significant reduction in the concentration of the NOx species. However, lean combustors are prone to transient flame holding phenomena, such as flame blowout. Flame instability is of great concern for aircraft engine designers because of reduced combustor efficiency and the potential for structural damage.

The large eddy simulation (LES) procedure received increased attention from the combustion research community in recent years due to its potential to accommodate realistic engineering configurations. Highly unsteady turbulent flows in complex combustor configurations need to be adequately solved. Since the flame is thinner than the characteristic integral scale in realistic industrial devices, the chemical reactions occur at the sub-grid scale (SGS) level and need to be modeled. Several approaches have been proposed for the treatment of premixed flames within the context of LES. One approach is the artificially-thickened flame model,[5,38] where the flame thickness is increased via the use of a increased value for the thermal diffusivity. Although this model is attractive for simulating complex chemistry and transient phenomena, it modifies the Damkohler number and can therefore lead to un-physical combustion dynamics. The level-set model is another approach, which attempts to model the premixed flame from a geometrical point of view. The level-set or G-equation, originally proposed by Williams,[40] models the evolution of the flame front. Several models have been developed based on the G-equation. Menon and his coauthors considered the level-set function as a progress variable.[3,19,24] This approach was applied successfully to realistic engineering problems.[8] Peters[28] proposed a transport equation for the level-set function treated as a distance function within the context of RANS. This approach was used by Nilsson and Bai[27] who also considered the effects of flame stretch in the flamelet model. Pitsch and Duchamp de Lageneste,[29] using LES, extended the level-set approach to include both the thin and corrugated flame regimes. Their numerical approach is based on a second-order finite volume method and an improved model for the turbulent burning velocity. The effects of mixing between the combustion products and the surrounding ambient on the flow field were also modeled. Huang et al.[14,15] considered the modeling approach of Pitsch and Duchamp de Lageneste[29] to study the combustion dynamics in a lean-premixed swirl-stabilized combustor. The LES equations were solved with a second-order finite volume method while the flamelet library used un-stretched premixed flames.

In the present work, we integrate a high-fidelity LES procedure with a level-set flamelet approach. The computational procedure is based on high-order spatial discretization of the governing equations. The compact, Padé approximation procedure[20] is used for low Mach number flows and weighted essentially non-oscillatory scheme[33] (WENO) for high Mach number flows. Thus, the high-fidelity simulation is available for all speeds, from incompressible to supersonic or even hypersonic speeds. The high-order spatial discretization is marched in time by a fourth-order Runge-Kutta procedure. In order to accommodate the analysis of realistic problems with complicated geometries and be competitive with unstructured mesh simulations, a matching high-order overset procedure was also developed and implemented. The implemented flamelet approach accounts for the effects of flame stretch and variable fuel-oxidizer mixing ratio. Our goal is to be able capable to accurately predict transient premixed and partially-premixed flame phenomena, including localized extinction and re-ignition in various turbulent reacting flow configurations. The foregoing capabilities in our procedure are needed for high-fidelity simulations of reacting flows in realistic combustor and augmentor geometries. The results of LES/level-set flamelet simulations presented here are validated with experimental measurements.

II. The Mathematical Models and Numerical Procedures

The transport equations for the filtered flow field variables, including those associated with combustion are presented in this section. The numerical procedures for the spatial and temporal discretization of the transport equations are also presented in this section.

A. The Governing Equations

The fully compressible forms of the continuity, momentum and energy equations are employed in this study since we are interested in the non-linear coupling between the acoustic, vorticity, and combustion fields. The Favre-averaged conservation equations are written in conservation form:[14]

$$\begin{aligned}
&\frac{\partial \bar{\rho}}{\partial t}+\frac{\partial\left(\bar{\rho}\tilde{u}_i\right)}{\partial x_i}=0,\\
&\frac{\partial\left(\bar{\rho}\tilde{u}_i\right)}{\partial t}+\frac{\partial\left(\bar{\rho}\tilde{u}_i\tilde{u}_j+\bar{p}\delta_{ij}\right)}{\partial x_j}=\frac{\partial\left(\tau_{ij}-\tau_{ij}^{SGS}\right)}{\partial x_j},\\
&\frac{\partial\left(\bar{\rho}\tilde{E}\right)}{\partial t}+\frac{\partial\left(\left(\bar{\rho}\tilde{E}+p\right)\tilde{u}_j\right)}{\partial x_j}=\frac{\partial\left(\tilde{u}_i\tau_{ij}-q_j+H_i^{SGS}+\sigma_j^{SGS}\right)}{\partial x_j}+S.
\end{aligned} \tag{1}$$

Here, $\bar{\rho}$ is the mass density, $\tilde{u}_i$ are the velocity components in the physical coordinate system (x,y,z), and $\tilde{E}$ is the total specific energy. Note that in Eq. (1), an overline over a variable implies Reynolds-averaging, while a tilde denotes Favre-averaging. In LES, the large scales motions are fully-resolved while the effects of the small scales are modeled. The separation between the large and small scales is determined by the grid size, Δ. In the system of transport equations (1), the filtered viscous stress tensor, τ_{ij}, and the heat flux vector, q_i, are based on the filtered flow variables. The sub-grid scale (SGS) terms, representing the effects of the small scale structures on the resolved scales, are

$$\begin{gathered}
\tau_{ij}^{SGS}=\overline{\rho u_i u_j}-\bar{\rho}\tilde{u}_i\tilde{u}_j,\quad \sigma_j^{SGS}=\overline{u_i\tau_{ij}}-\tilde{u}_i\overline{\tau_{ij}},\\
H_i^{SGS}=\overline{\rho E u_i}-\bar{\rho}\tilde{u}_i\tilde{u}_j+\overline{pu_i}-\bar{p}\tilde{u}_i.
\end{gathered} \tag{2}$$

The unclosed viscous work, σ_j^{SGS}, is assumed to be small and is neglected in the present work. The SGS contribution to the shear stresses, τ_{ij}^{SGS}, is computed using the Smagorinsky model.[35] The model parameters are determined empirically, or are dynamically computed as a function of local flow conditions using the formulation of Germano et al.[12] and Moin et al.,[25] with the modification proposed by Lilly.[21] The SGS energy flux, H_i^{SGS}, is modeled as

$$H_i^{SGS} = -\bar{\rho}\,\frac{\nu_t}{\Pr_t}\left(\frac{\partial \tilde{h}}{\partial x_i} + \tilde{u}_j\,\frac{\partial \tilde{u}_j}{\partial x_i} + \frac{1}{2}\,\frac{\partial k^{SGS}}{\partial x_i}\right). \tag{3}$$

Here $\tilde{h}$ is the filtered specific enthalpy. The turbulent Prandtl number in Eq. (3), Pr_t, can be considered either constant, or can be dynamically computed[21,25] during the simulation.

The filtered total specific energy is given as

$$\tilde{E} = \int_{T_0}^{\tilde{T}} c_p\,dT - \frac{\bar{p}}{\bar{\rho}} + \frac{\tilde{u}_i\tilde{u}_i}{2} + k^{SGS}. \tag{4}$$

The source term in the energy transport equation, S in Eq. (1), accounts for the chemical heat release and is outlined in section III.A.

B. Spatial Discretization and Temporal Integration

In order to facilitate the numerical simulation of flow configurations around arbitrary complicated bodies, the transport equations need to be re-cast for a generalized curvilinear coordinate system. In order to facilitate this conversion, the system of transport equations is written in vector form as:

$$\frac{\partial Q}{\partial \tau} + \frac{\partial F}{\partial x} + \frac{\partial G}{\partial y} + \frac{\partial H}{\partial z} = \frac{\partial F_v}{\partial x} + \frac{\partial G_v}{\partial y} + \frac{\partial H_v}{\partial z} + S\,, \tag{5}$$

where Q is the vector of conserved variables, $Q = (\rho, \rho u, \rho v, \rho w, \rho E)^T$, (F,G,H) are the convective fluxes, (F_v,G_v,H_v) are the viscous fluxes, and S is the source term, which is non-zero only in the energy transport equation (in the expressions above, the "~" notation was dropped for simplicity). In the curvilinear coordinate system (ξ,η,ζ), Eq. (5) are written as

$$\frac{\partial (Q/J)}{\partial t} + \frac{\partial \hat{F}}{\partial \xi} + \frac{\partial \hat{G}}{\partial \eta} + \frac{\partial \hat{H}}{\partial \zeta} = \frac{\partial \hat{F}_v}{\partial \xi} + \frac{\partial \hat{G}_v}{\partial \eta} + \frac{\partial \hat{H}_v}{\partial \zeta} + \hat{S}\,, \tag{6}$$

where J is the Jacobian of the transformation between the generalized coordinate system (ξ,η,ζ) and physical coordinate system (x,y,z). The convective flux in the computational ξ-direction in Eq. (6) is given by

$$\hat{F} = \frac{1}{J}\left(\xi_x F + \xi_y G + \xi_z H\right). \tag{7}$$

The expressions for the other convective and viscous fluxes are similar. The transformed source term in Eq. (6) is computed as $\hat{S} = S / J$.

High-order compact finite differences are used to discretize the convective and diffusive fluxes in Eq. (6) for low Mach number flows. Consider the differencing of a variable ϕ (e.g. conserved variable, flux component, etc.) along the ξ direction, that is $\phi' = \partial\phi / \partial\xi$. An implicit, centered finite difference formula is employed to calculate ϕ':[20]

$$\alpha\phi'_{i-1} + \phi'_i + \alpha\phi'_{i+1} = b\,\frac{\phi_{i+2} - \phi_{i-2}}{4\Delta\xi} + a\,\frac{\phi_{i+1} - \phi_{i-1}}{2\Delta\xi}\,. \tag{8}$$

The parameters α, a, and b determine the spatial accuracy of the algorithm and their values are determined using Taylor series expansions around point i. For a sixth-order accurate scheme, $(\alpha, a, b) = \left(1/3, 14/9, 1/9\right)$.[11,20]

Compact finite differences are non-dissipative and are susceptible to nonlinear instabilities. In order to remove high frequency noise and maintain solution integrity, a low-pass filtering procedure is adopted. For a typical component of the solution vector, ϕ, the filtered values $\tilde{\phi}$ are obtained from

$$\alpha_f\,\tilde{\phi}_{i-1} + \tilde{\phi}_i + \alpha_f\,\tilde{\phi}_{i+1} = \sum_{k=0}^{N} \frac{a_k}{2}\left(\phi_{i+k} + \phi_{i-k}\right). \tag{9}$$

The coefficients a_k are expressed in terms of α_f, which is a parameter that controls the strength of the filter. As α_f is reduced, a wider band of high frequencies is damped. The range $0.3 \le \alpha_f < 0.5$ has been suggested.[39]

For high-order differencing of flow fields with shock waves, the characteristic-wise weighted essentially non-oscillatory (WENO) procedure is used (see Shu,[33] procedure 2.10). This numerical approach is summarized below.

Considering the ξ -direction as an example, we have

$$\left.\frac{\partial \hat{F}}{\partial \xi}\right|_i = \frac{1}{\Delta \xi}\left\{\left[\tilde{R}_{Roe}\cdot\left(\tilde{R}^{-1}_{Roe}\cdot\hat{F}\right)\right]_{i+1/2} - \left[\tilde{R}_{Roe}\cdot\left(\tilde{R}^{-1}_{Roe}\cdot\hat{F}\right)\right]_{i-1/2}\right\}, \tag{10}$$

where $\tilde{R}_{Roe}$ is the matrix formed with the right eigenvectors of the Jacobian $\partial\hat{F}/\partial Q$ computed based on a Roe-averaged state at *i±1/2*. For the characteristic-wise WENO, the reconstruction procedure is performed on the characteristic fields $\hat{F}_c = \tilde{R}^{-1}_{Roe}\cdot\hat{F}$ to obtain the values at $i+1/2$. The Lax-Friedrichs flux-splitting method is used to obtain the left and right states at the mid-points:

$$\hat{F}^{\pm}_c = \frac{1}{2}\left(\hat{F}_c \pm \alpha q\right), \tag{11}$$

where α is the spectral radius of the Jacobian $\partial\hat{F}/\partial Q$. The characteristic-wise fluxes at the mid-points are reconstructed as

$$\hat{F}^{+}_{c,i+1/2} = \sum_{r=0}^{k-1}\omega_r F^{(r)+}_{c,i+1/2},\; \hat{F}^{-}_{c,i+1/2} = \sum_{r=0}^{k-1}\tilde{\omega}_r F^{(r)-}_{c,i+1/2},\; F^{(r)}_{c,i+1/2} = \sum_{m=0}^{k-1} c_{rm}\hat{F}_{c,i-r+m}\ , \tag{12}$$

where ω_r and $\tilde{\omega}_r$ are normalized weights (see Shu,[33] section 2.2.2), based on smoothness indicators of the numerical fluxes and c_{rm} are the coefficients of Lagrange interpolation. Finally, the reconstructed characteristic fluxes are converted back to physical space, $\hat{F}^{\pm}_{i+1/2} = \tilde{R}_{Roe}\cdot\hat{F}^{\pm}_{c,i+1/2}$, and the numerical flux formed as

$$\hat{F}_{i+1/2} = \hat{F}^{+}_{i+1/2} + \hat{F}^{-}_{i+1/2}. \tag{13}$$

The viscous fluxes for high Mach number flows are discretized high-order compact finite differences.

Due to the strong interaction between the flow field and the flame, accurate time-dependent solutions are required. In order to achieve this accuracy, the classical fourth-order Runge-Kutta scheme is employed in its low-storage form[10] for time integration of the system of transport equations in Eq. (6).

C. The Laminar Flamelet Approach

The effect of chemical heat release on the flow field is computed via a laminar flamelet model. The main idea behind this approach is the assumption that a turbulent flame is a collection of laminar flamelets embedded in an otherwise inert turbulent flow. The flame inner structure can be calculated independent of the turbulent flow, using arbitrary detailed kinetic models and realistic multi-species transport properties. The limitations of this approach are well known.[2]

The freely-propagating premixed flame configuration and the opposed jet configuration are two canonical configurations widely used to generate model data for flamelet libraries. For these configurations, the flame structure is assumed to be one-dimensional, which leads to some simplifications of the multi-species transport equations. The governing equations are given elsewhere.[17,23] The freely-propagating flame configuration is used to determine the laminar flame velocity, $S_{L,0}$, for various fuel-to-oxidizer equivalence ratio, Φ, and reference ambient pressure values. In the second configuration, a stretched flame is formed between two opposing jets. Depending on the jet mixture set-up, the flame can be premixed, partially-premixed, or non-premixed. The flame stretch-rate, K, is controlled by adjusting the velocities of the opposing jets. Flamelet libraries are constructed by tabulating the flame data such as species mass fractions, Y_i, reaction rates, $\dot{\omega}_i$, etc. as functions of G and K for various values of Φ. Here, G is the distance from an arbitrary point in the domain to the flame surface.

The turbulent flame characteristics are computed under the assumption that the turbulent flame is an ensemble of different laminar flamelets that fluctuate randomly around the mean flame location. Assuming that the joint PDF *P(G,K)* is known, the Favre-averaged reaction rates can be computed as:

$$\tilde{\dot{\omega}}_k = \frac{1}{\bar{\rho}}\iint \rho\left(G-\tilde{G}(\vec{x}),K\right)\cdot\dot{\omega}_k\left(G-\tilde{G}(\vec{x}),K\right)\cdot P(G,K)\,dG\,dK. \tag{14}$$

Assuming statistical independence, *P(G,K)* is assumed to be a product of a Gaussian distribution for the flame distance function[14] and a log-normal distribution for the flame stretch rate.[1] This model can account for partial extinction of the premixed turbulent flame when local stretch rate becomes larger than the extinction limit, K_{ext}.

D. The Level-Set Equation

The evolution of Favre-averaged *G*, or $\widetilde{G}$, is modeled by a level-set equation:[28]

$$\frac{\partial\left(\overline{\rho}\widetilde{G}\right)}{\partial t}+\frac{\partial\left(\overline{\rho}\widetilde{u}_i\widetilde{G}\right)}{\partial x_i}=\overline{\rho}S_T\left|\frac{\partial\widetilde{G}}{\partial x_i}\right|-\overline{\rho}D_t\widetilde{\kappa}\left|\frac{\partial\widetilde{G}}{\partial x_i}\right|, \tag{15}$$

where S_T is the turbulent burning velocity, D_t is the turbulent diffusivity, $D_t=\nu_t/\mathrm{Pr}_t$, and $\widetilde{\kappa}$ is the curvature of the flame surface, $\widetilde{\kappa}=\nabla\cdot\left(-\nabla\widetilde{G}/\left|\nabla\widetilde{G}\right|\right)$. The turbulent flame velocity is modeled as[22]

$$S_T=S_L\left(1+C\left(\frac{u'}{S_L}\right)^n\right), \tag{16}$$

where *C~2.0*, *n~0.7*, and u' is the SGS turbulent velocity fluctuation, which is assumed to be $u'=2\Delta^3\left|\nabla\times\nabla^2\widetilde{\widetilde{u}}\right|$.

High-order ENO discretization[13,31,32] is used to discretize the spatial derivates in Eq. (15), with local Lax-Friedrichs flux-splitting, to ensure a robust evaluation of the convection term in this equation. The time marching is performed using 2nd and 3rd order TVD Runge-Kutta schemes. Equation (15) is only valid at the flame front, $\widetilde{G}=0$. Since the distance function property of $\widetilde{G}$ is not preserved by the level-set equation, this condition needs to be enforced through a re-initialization procedure. For this purpose, we use the procedure of Sussman et al.[37] with the extension in Russo and Smerenka.[30] This procedure involves solving the following equation to steady state:

$$\frac{\partial G}{\partial\tau}=\mathrm{sgn}(G_0)(1-|\nabla G|),\ G(x,0)=G_0(x). \tag{17}$$

Here, $\mathrm{sgn}(\cdot)$ is the sign function. The "~" was dropped from the flame distance function to simplify the notation. Due to the hyperbolic nature of Eq. (17), the characteristics propagate outward from the zero level, $\widetilde{G}=0$. Since the flame thickness is small compared to the large scale structures, Eq (17) is advanced towards the steady state only for a limited region around the flame surface. The narrow band method[16] has been implemented to ensure the computational efficiency of the re-initialization procedure.

In order to discretize the spatial derivatives, Eq. (17) is written in the form

$$\frac{\partial G}{\partial\tau}+\vec{w}\cdot\nabla G=\mathrm{sgn}(G_0),\ \ \vec{w}=\mathrm{sgn}(G_0)\cdot\nabla G/|\nabla G|. \tag{18}$$

Here, $\vec{w}$ is the unit velocity vector pointing away from surface $G_0=0$. In curvilinear coordinates, the partial derivative of the level-set function is computed as

$$\frac{\partial G}{\partial x}=J\left(\left(\frac{\xi_x}{J}G\right)_\xi+\left(\frac{\eta_x}{J}G\right)_\eta+\left(\frac{\varsigma_x}{J}G\right)_\varsigma\right). \tag{19}$$

The expressions for the other partial derivatives are similar. Metric identities (Visbal and Gaitonde[39]) were used to derive the conservative form in Eq. (19). The convection term in Eq. (18) is further expanded as

$$\vec{w}\cdot\nabla G=W_\xi G_\xi+W_\eta G_\eta+W_\varsigma G_\varsigma, \tag{20}$$

where W_i are the contravariant velocities, defined by

$$\begin{aligned}W_\xi&=w_x\xi_x+w_y\xi_y+w_z\xi_z,\\W_\eta&=w_x\eta_x+w_y\eta_y+w_z\eta_z,\\W_\varsigma&=w_x\varsigma_x+w_y\varsigma_y+w_z\varsigma_z.\end{aligned} \tag{21}$$

Since the characteristic lines are pointing away from $G_0=0$, it is therefore natural to use an upwinding procedure to calculate the convection term (Sussman, Smereka, and Osher[37]). In Cartesian coordinates, the upwind algorithm is based directly on the components of ∇G. However, we have found that the upwind algorithm based directly on the partial derivatives G_{ξ_i} is less robust in a curvilinear coordinate system, especially for locally skewed meshes. Instead, we computed the contravariant velocities W_i using central finite differences for the rhs terms in Eq. (21). Then we applied the upwind algorithm for the partial derivatives of G in Eq. (20), based on the local values of the contravariant velocities.

III. Results

The numerical features described in the previous section have been implemented into AEROFLO, which is a CFD software product developed by Thaerocomp Technical Corp. The aim of the combined high-order LES/level-set flamelet approach is to accurately predict transient flame phenomena and the detailed coupling between flow and combustion instabilities. A detailed description of the validation of the flamelet library, the level-set algorithm, and the coupled LES/Flamelet approach is presented in this section.

A. Flamelet Library

The laminar flame data used in our flamelet library was validated against experimental results and the predictions from the well-established Chemkin II software.[17,18,23] Fig. 1 shows comparisons between the results obtained from the freely-propagating flame module of AEROFLO, Chemkin II, and experiments. Both detailed methane kinetics (GRI-Mech 3.0[34] with 53 species and 325 elementary reactions), and reduced kinetics (DRM22[16] with 24 species and 104 elementary reactions) were calculated. The Chemkin II results are generated using GRI-Mech 3.0. A good agreement for the laminar flow velocity, $S_{L,0}$ between the AEROFLO results and the other numerical and experimental values is observed. Since the detailed chemistry results in Fig. 1(a) are in better agreement with the experimental values, only the detailed chemistry calculations are shown in Fig. 1(b) and throughout the rest of this paper.

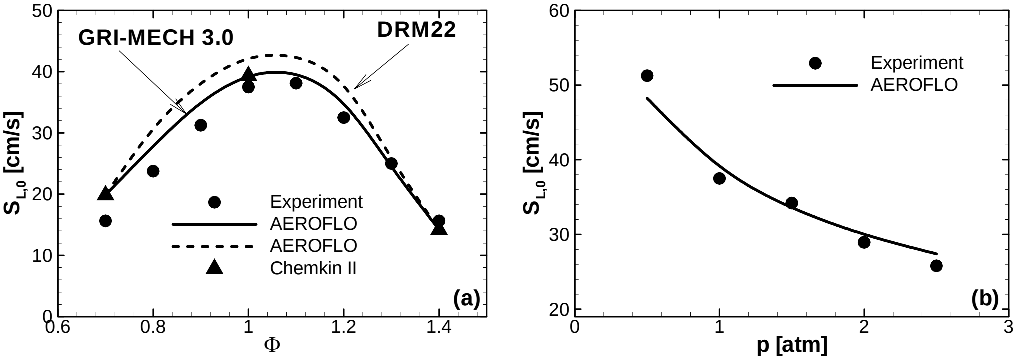

Fig. 1 Comparison of laminar flame velocity values for (a) lean/rich conditions, and (b) low and elevated values of the ambient pressure.

Sample results obtained with the opposed-jet module of AEROFLO are compared with Chemkin II predictions in Fig. 2. These results correspond to a stoichiometric methane-air flame. An excellent agreement between AEROFLO and Chemkin II is evident for both the major species and the radicals. In this figure, $G = 0$ corresponds to the flame surface, defined as the location of the peak heat release rate.

The chemical source term, Q_T^0, is defined as

$$Q_T^0 = -\sum_{i=1}^{N_s} \dot{\omega}_i \Delta h_{f,i}^0 , \tag{22}$$

where $\dot{\omega}_i$ is the molar reaction rate of species *i*, $\Delta h_{f,i}^0$ is the enthalpy of formation of species *i*, and N_s is the total number of species in the kinetic model. Typical chemical source term profiles corresponding to several flame stretch rates are shown in Fig. 3(a) for a stoichiometric methane-air mixture. Note that the opposed-jet configuration allows the construction of flame data near extinction.

The filtered chemical source term in the total energy transport equation (1) is defined as

$$S = \iint P(G,K) Q_T^0 dG dK \, . \tag{23}$$

The probability density functions (PDFs) of the flame distance and stretch rate are assumed to be statistically independent. A Gaussian distribution is assumed for the probability of the flame location. The turbulent flame thickness, $l_{F,t} = \sqrt{\left.\overline{G''^2}\right|_{\tilde{G}=0}}$, is required for the evaluation of the PDF of *G*. In this study, the turbulent flame thickness is modeled as $l_{F,t} = l_F + \Delta$, where l_F is the laminar flame thickness and Δ is the local grid size. Following Abdel-Gayed et al.[1] and Nilsson and Bai,[27] a log-normal distribution is assumed for the stretch rate. For this approach, the turbulent stretch rate is modeled based on the sub-grid scale dissipation similar to Flohr and Pitsch.[9]

Fig. 3(b) shows the effect of the grid size, Δ, for a model stretch rate of *K*=500/s. Similar profiles have been obtained for other stretch rate values (from zero to extinction). In order to save on the computational time, the chemical source term is filtered in a pre-processing routine and stored in a flamelet table as a function of *G*, *K* and Δ. During the simulation, the contribution of the chemical heat release in the energy equation is evaluated through a multi-dimensional interpolation in the flamelet table.

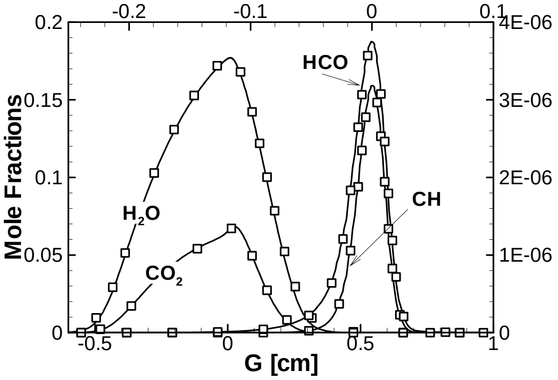

Fig. 2 Sample major and minor species profiles in an opposed-jet configuration; comparison between AEROFLO (solid lines) and Chemkin II (symbols). The left profiles correspond to the left and bottom axes, while the right profiles correspond to the right and top axes.

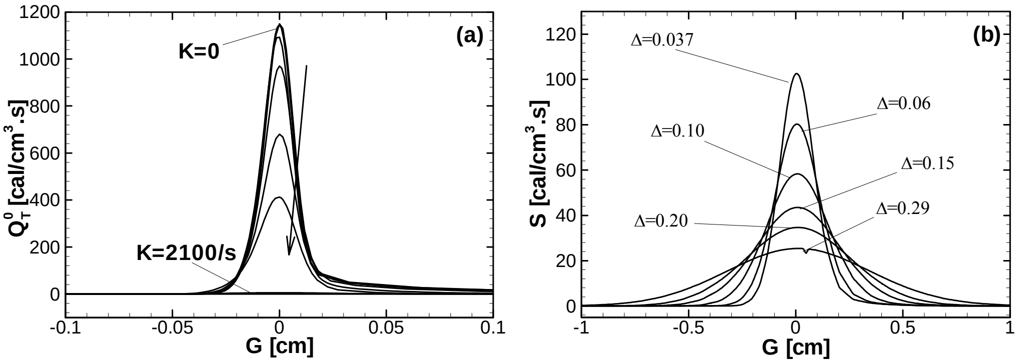

Fig. 3 (a) The distribution of the chemical source term for various values of the stretch rate *K*, and (b) filtered values corresponding to *K*=500/s for various values of the grid size. The arrow in (a) shows the direction of increasing stretch rates.

B. Level-Set Algorithm

The advection/rotation/re-initialization procedures for level-set functions were tested for canonical configurations. In order to rigorously test the robustness and accuracy of the level-set function transport and re-initialization algorithms presented in Section II.D, a highly skewed curvilinear mesh, shown in Fig. 4, was used.

In the first test, the $G_0 = 0$ level is an ellipsoid with the center located in the middle of the computational domain. A uniform velocity of unit magnitude is imposed in the physical *x*-direction. The results at $t = 24$, in Fig. 5(a), show overlapping $G_0 = 0$ levels at symmetric $y = const$ planes with respect to the center of the computational domain. Moreover these surfaces maintained their initial ellipse shape.

For the second test, the $G_0 = 0$ level corresponds to a rectangle in $z = const$ planes. For this case, shown in Fig. 5(b), the velocities correspond to a rigid body rotation in the counterclockwise direction. The rectangular shape of the level set function is well preserved during the rotation motion, even on the highly skewed mesh. The results shown in Fig. 5 confirm the accuracy of the level-set procedure. For both the advection and the rotation cases, additional tests (not shown) were performed to determine the optimal number of re-initialization iterations. It was found that 10-30 re-initialization steps were required to obtain accurate results, with the larger value corresponding to highly-skewed computational meshes.

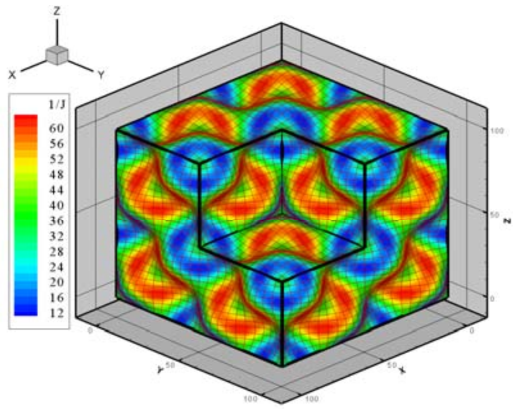

Fig. 4 Jacobian values for a curvilinear mesh with 31^3 nodes used to test the level-set algorithms. Some grids were blanked to enhance the view.

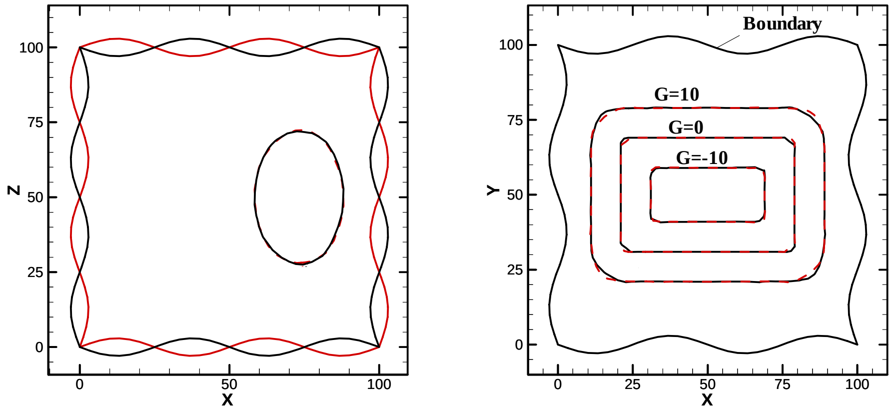

Fig. 5 (a) Sections at *y=30* (solid lines) and *y=70* (dashed lines) through the ellipsoid at t=24, and (b) rectangle-shaped level-set functions at *t=0* (solid contours) and after one full rotation (dashed lines).

The computation of the curvature, $\tilde{\kappa}$, which is required in Eq. (15), involves the evaluation of second-order derivatives of the level-set function. This can lead to erroneous results in regions with large curvature variations and non-orthogonal computational meshes. A series of comparisons between various numerical evaluations of the curvature and analytical expressions for a unit sphere (results not shown) indicate that 6th-order schemes (ENO or compact) are necessary to obtain accurate results. These comparisons also indicate that 4th order schemes are sufficient only for orthogonal and moderately skewed meshes only.

C. LES of a V-Gutter Flame Holder

A combined numerical and experimental investigation was conducted on a flame holder configuration. Figure 6(a) is a schematic of the experimental configuration. A 12MW experimental combustion facility located at the Propulsion Directorate of Air Force Research Laboratory in Wright-Patterson Air Force Base, Dayton, Ohio was used for the experiments. The facility is capable of simulating the exit conditions of the Low Pressure Turbine (LPT) of legacy, pipeline and future high performance fighters. Flow conditioning is employed in the facility which provides a uniform velocity and temperature profile (± 3%), and 6% turbulence at the inlet of the test section. The flame holder is a v-gutter-type bluff-body which traverses the height of the test section (*z*-direction not shown in the figure). In this configuration, the flow is considered two-dimensional at the center of the test rig.

A six-block overset computational grid, shown in Fig. **6**(b), was generated for this problem. Table I shows the number of grid points in each block. The grid lines in blocks 1 through 4 are distributed to ensure a sufficient number of grid points in the vicinity of the v-gutter. For blocks 5 and 6, the grid lines conform to the specific wall topology, to better capture the boundary layer that develops on the flame holder. This is necessary in order to obtain a correct vortex shedding pattern downstream of the bluff-body.

Block	No. of grid points	Grid size Min	Grid size Max
1	7696	0.02	0.08
2	8140	0.02	0.10
3	7696	0.02	0.08
4	8140	0.02	0.10
5	7425	3×10^{-4}	0.14
6	7425	3×10^{-4}	0.14

Table I. Computational grids. The grid dimensions have been normalized with the v-gutter width.

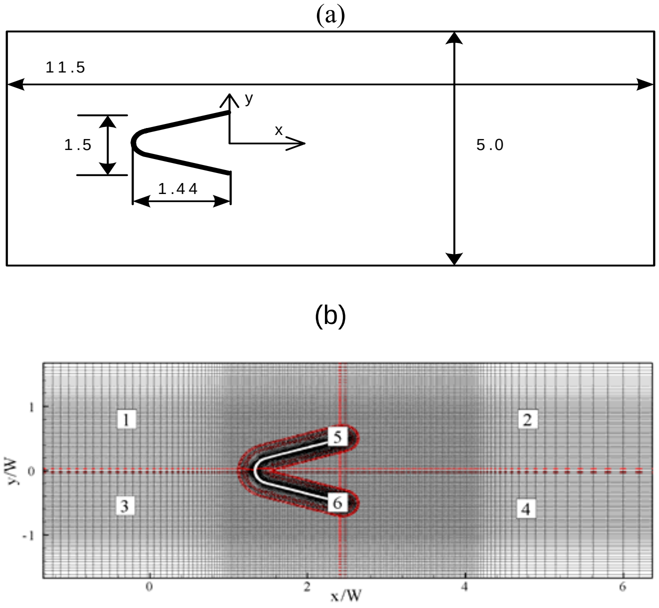

Fig. 6 (a) Schematic of a 2D section through the experimental configuration, and (b) rectangle-shaped level-set functions at t=0 (black contours) and after one full rotation (red lines).

An overset grid procedure is employed to exchange information between blocks 5 and 6 and the other computational blocks (see Fig. 7). The number of overlap grid points used between these blocks ensures that the order of the compact scheme in the interior computational domain is maintained across the boundaries.

The boundary conditions for LES are set to match the experimental conditions. The gradient of pressure is zero while the density and velocities are prescribed at the inflow (left boundary in Fig. **6**(b)). The Reynolds number based on the inflow streamwise velocity and the v-gutter width is 29,000 and the Mach number is 0.15. The inflow transverse velocity component is set to zero. At the outflow, zero-gradient conditions are prescribed for all variables, except pressure, whose value is imposed. Periodic conditions are imposed in the transverse direction for the bottom and top boundaries in Fig. 6(b).

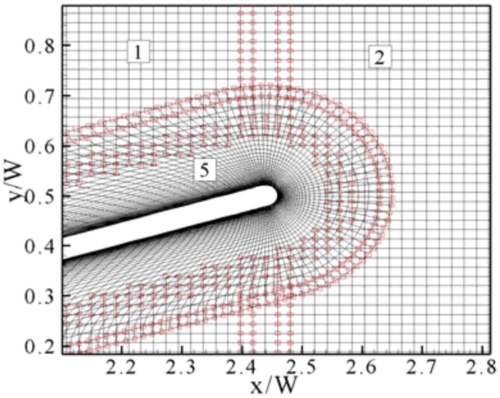

Fig. 7 Computational grid detail near the upper trailing edge. The red squares indicate overset boundary nodes.

The computational domain is initially quiescent. A symmetric recirculation region forms downstream of the v-gutter at early times (results not shown). At later times, the numerical flow field loses its symmetric character due to small numerical instabilities and a vortex-shedding pattern develops. Thus, no explicit forcing was used to initiate vortex-shedding. Fig. 8 is representative of the clockwise and counterclockwise vortex shedding behind the v-gutter. In this figure, two dominant coherent vortex structures can be seen. These are large periodic vortices of opposite sign on the order of the scale of the v-gutter. These large-scale structures appear to be the von Karman vortices typical of the shedding behind a bluff-body.

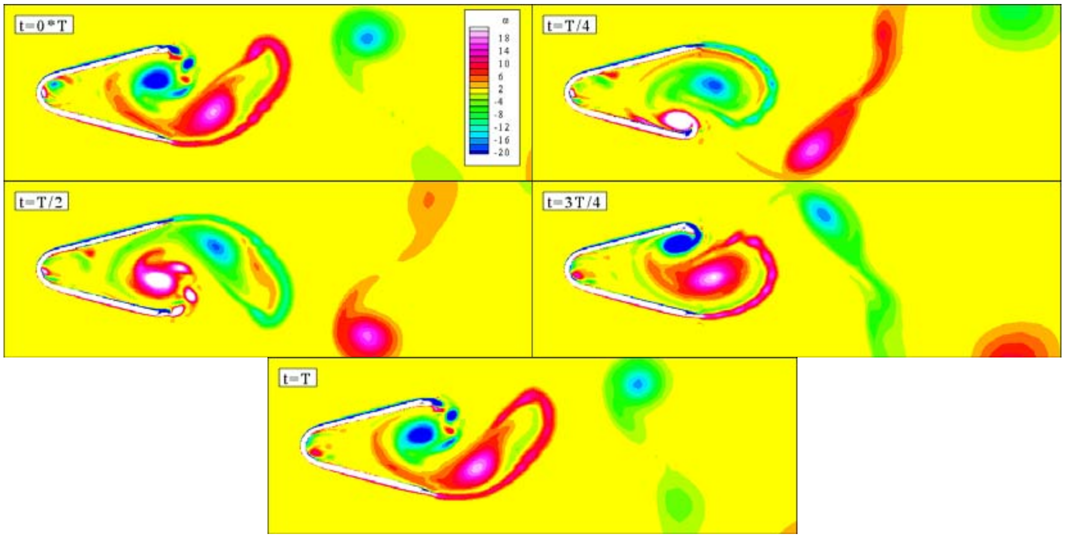

Fig. 8 Vortex shedding behind the v-gutter

There are also trails of smaller vortices that originate at the v-gutter trailing edges. As the larger vortices are formed inside the v-gutter, their circulation creates appreciable velocity along the inner wall of the v-gutter. The rotation of the clockwise vortex produces positive velocity on the upper inside wall while the counter clockwise vortex produces positive velocity on the lower v-gutter wall. This velocity results in a boundary layer that grows on the inside surfaces of the v-gutter. The inner boundary layer meets with the outer boundary layer at the trailing edge of the v-gutter and vortices that appear to be of the Kelvin-Helmholtz type are formed. These vortices quickly curl around as the large coherent vortex spins. Due to their scale they are quickly dissipated and are therefore short-lived in the flow.

In order to confirm the shedding frequency for the Karman vortices, LDV and LES data were taken in the wake of the v-gutter. Figure 9(a) depicts the FFT of the LES velocity data 1/3 of a gutter width downstream of the flame holder at three transverse positions in the wake. In this figure, the dominant amplitude occurs at a frequency of 334Hz for all three signals. This value corresponds to a Strouhal number, $St=0.24$. In addition, the signals from the off-center locations, $y=\pm 0.5$ in., exhibit a second dominant frequency, which corresponds to a Strouhal number, $St_2=0.54$. This frequency is associated with the smaller vortices generated from the v-gutter trailing edges.

(a) (b)

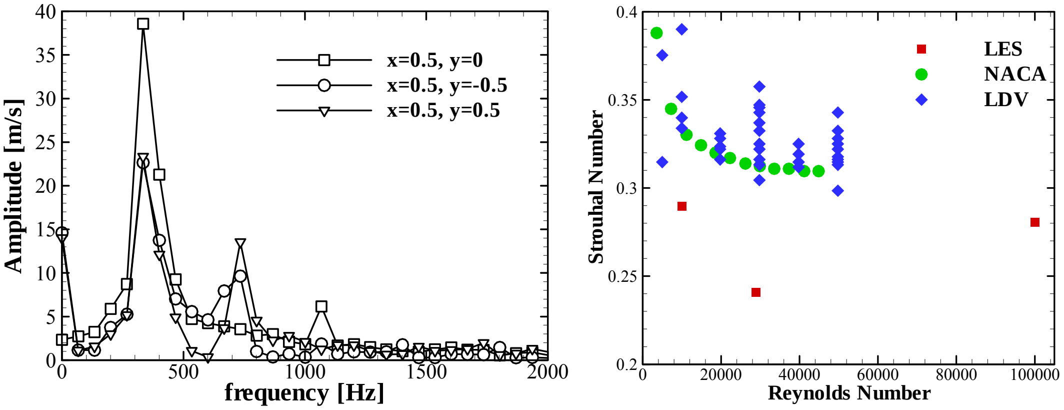

Fig. 9 (a) Dominant shedding frequencies for the v-gutter flame holder and (b) comparison of experimental and numerical Strouhal numbers at several Reynolds numbers.

Several more computational and experimental "runs" were made over many different Reynolds numbers. LDV experiments were conducted at five different inlet Reynolds numbers ranging from 4,968 to 49,681, while the Reynolds Numbers in the LES ranged from 10^4 to 10^5. Figure 9(b) is a plot of the Strouhal data collected for all of the Reynolds numbers tested and the data for a 30 degree 0.75 inch v-gutter from NACA RM E51K07.[41] Note that the Strouhal data for the v-gutter from LDV compares very well with the NACA results. The Strouhal number values from the numerical simulations are approximately 7-20% lower than the equivalent experimental results for the lower Reynolds Numbers. Further investigation is needed to understand the differences between the experimental data and the results of the numerical simulations.

D. LES/Level-Set Flamelet Simulation of a Turbulent Bunsen Burner

A 2D LES/Level-Set Flamelet study was carried out to validate the combustion simulation tools presented in this paper. The characteristics of established flame data are being calculated and compared for the Bunsen burner configuration of Chen et al.[4] This configuration was also used by Pitsch and Duchamp de Lageneste[29] to test the level-set model in their LES procedure. Fig. 10 shows a schematic of the experimental configuration and the computational domain. The boundary $x = 0$ in Fig. 10(b) corresponds to the pilot flame and main jet exit plane in Fig. 10(a). The pilot stream extends from $y/D = -2.8$ to $y/D = 2.8$ at $x = 0$ to match the experimental specifications. The 2D computational mesh uses *141×101* grid points and spans *30D* and *20D* in the streamwise and transverse directions, respectively. The grid lines are clustered in the transverse direction near the expected flame region and in the streamwise direction near the jet exit plane to accurately capture the interaction between the pilot flame and the initially cold premixed mixture. The total number of grid points is deliberately kept small compared to similar LES studies to test the ability of the high-fidelity numerical scheme to capture the main features of the turbulence-chemistry interaction with a coarse grid.

The boundary conditions were set to match the experimental conditions for Flame F3 of Chen et al.[4] These conditions correspond to an inlet velocity of 30 m/s and a Reynolds number, *Re*=23,500 for the premixed mixture jet. Based on the experimental findings, F3 is well within the flamelet regime for which the current approach was designed. Fig. 11 shows contour plots of the normalized temperature field for a reacting LES simulation. For this simulation, the pilot flame is assumed to generate hot combustion products right before $x = 0$. Due to the heat released by the consumption of the fresh mixture in the jet, the shear layer expands in the radial direction in qualitative agreement with the experimental observations.

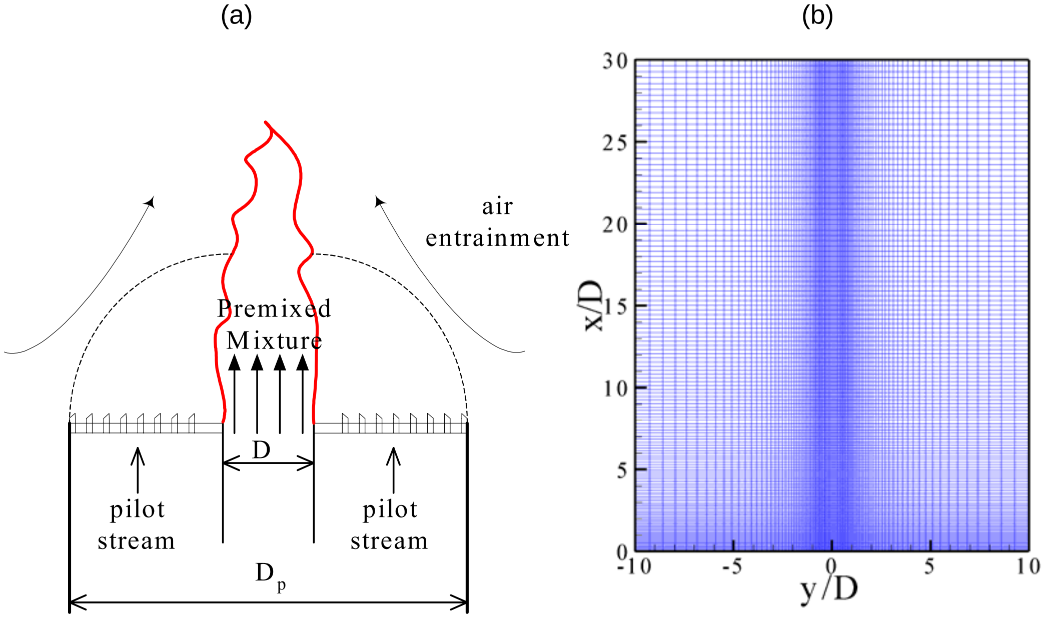

Fig. 10 (a) Schematic of the Bunsen burner experimental setup and (b) 2D computational grid used for the computational study.

The average streamwise velocity and temperature profiles for a reacting simulation are shown in Fig. 12. A very good agreement with the experimental results is evident at *x/D=2.5* and *x/D=4.5*. At locations further downstream, the temperature near the centerline exhibits a local maximum in the numerical simulations, a phenomenon that is not observed in the experiments. This difference is due to a curved region in the flame surface shape (see Fig. 11, close to $x = 0$). This curvature leads to a flame surface located closer to the centerline, $y = 0$, compared to the experiments. Comparison of the species mass fractions for select major species and radicals in Fig. 12 reveals a similar shift towards the centerline for the numerical results compared to the experimental data.

We are currently extending the computational domain to also simulate the flow upstream of the jet exit plane to correct this behavior. Also, we are in the process of implementing a transport equation to model the passive mixing between the combustion products and the surrounding ambient, and of testing a more comprehensive turbulent burning velocity model by Pitsch and Duchamp de Lageneste.[29]

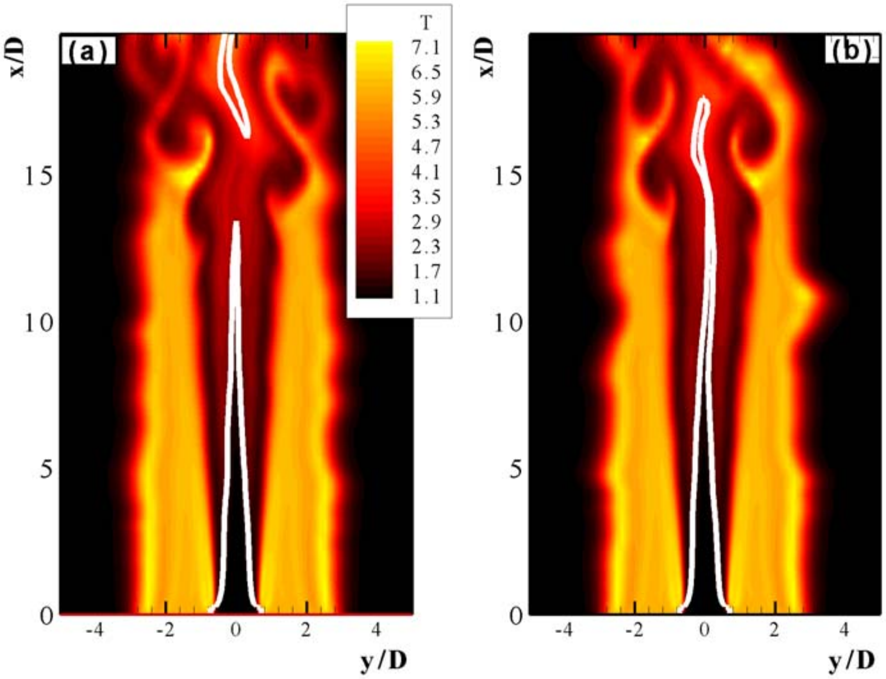

Fig. 11 Instantaneous filtered temperatures contour plots for the turbulent Bunsen burner configuration. The flame surface is shown with thick white contours. The time interval between (a) and (b) is approximately 2 flow-through times.

IV. Conclusions

In this paper we reported on the validation of a high-fidelity flamelet-based code with the capability to predict unsteady premixed flame behaviors such as local extinction and re-ignition. The presented results indicate that the proposed procedures are robust and quite viable from accuracy and efficiency stand points.

The flow solver incorporates high-order spatial and time differencing techniques coupled with a matching high-order overset procedure to permit the analysis of realistic problems which usually have very complex geometries. The coupling between chemical reaction and the flow field is achieved through a level-set flamelet approach. The laminar flamelet library has been generated with a code developed in-house using detailed kinetic models and realistic multi-species transport and thermodynamic properties. The flamelet data are validated through comparisons with experimental results and results from other numerical simulations. A level-set transport and re-initialization algorithm was implemented in curvilinear coordinates to accommodate complex geometries.

Non-reacting and reacting simulations using LES and a relatively small number of grid nodes have been performed to verify the ability of the developed software to capture the turbulent flow and combustion characteristics. A good agreement with the experimental data is reported. Future work includes the incorporation of additional models for the turbulent burning velocity.

Acknowledgments

This contribution from Thaerocomp Technical Corp. to this work was funded by the United States Air Force, Contract FA8650-04-C-2496, via the Phase II SBIR Program. The authors are very grateful to the Air Force for giving Thaerocomp the opportunity to develop innovative research tools for augmentor simulation.

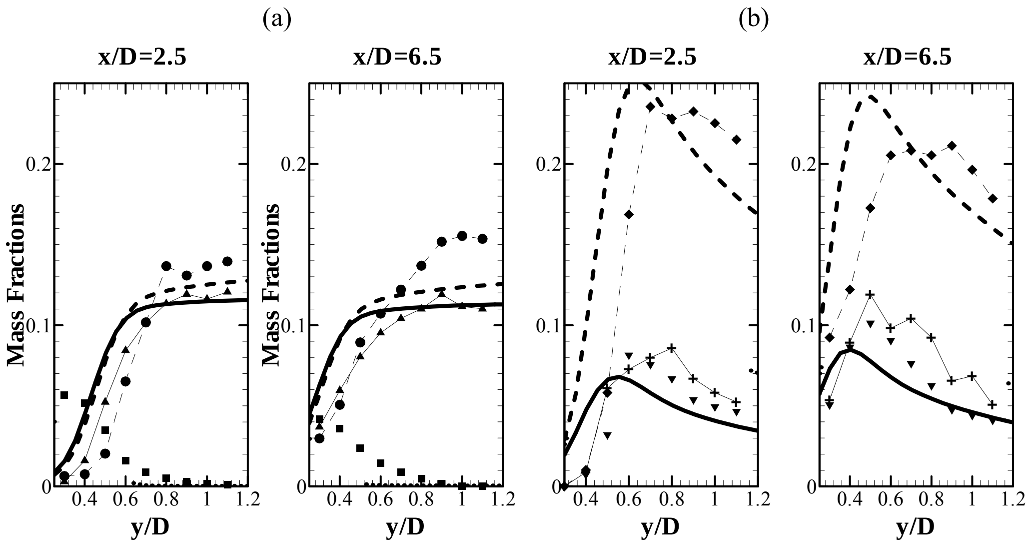

Fig. 12 Comparison of mean species mass fraction values for (a) CH_4 (dotted line and square), CO_2 (dashed line and triangle), H_2O (solid line and triangle), and (b) OH (dashed line and diamond), H_2 (solid line and "+"), CO (dottet line and gradient). The thick lines correspond to the numerical simulation and the thin lines and symbols correspond to the experimental data. The mass fractions values for OH were multiplied with 75, for H_2 with 100, and for CO with 10.

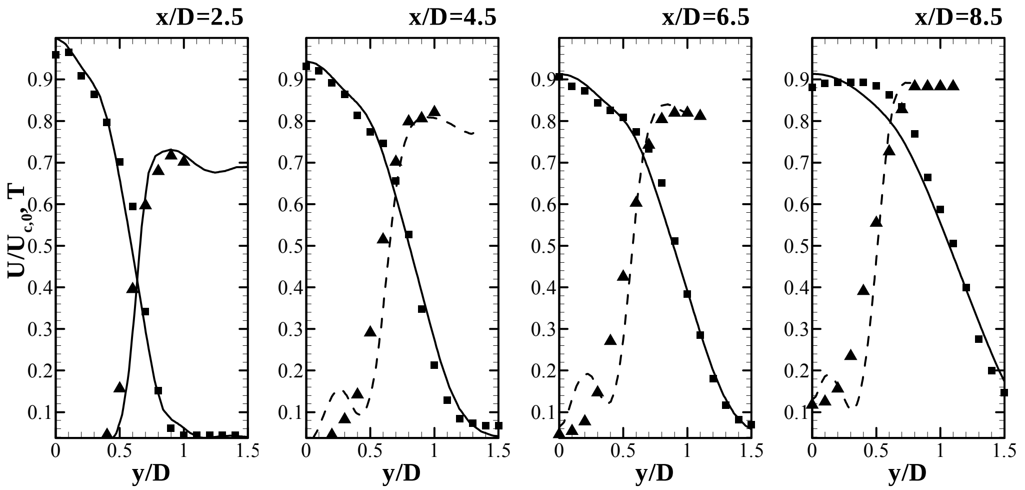

Fig. 13 Mean streamwise velocity (solid lines and squares) and temperature (dashed lines and triangles) at various locations across the flame. The lines correspond to LES/Flamelet results and the symbols to the experimental data.

References

[1] Abdel-Gayed, R. G., Bradley, D., and Lau, A. K. C., "The Straining of Premixed Turbulent Flames," *Proceedings of the Combustion Institute*, Vol. 22, 1988, pp. 731-738.

[2] Buckmaster, J., Clavin, P., Linan, A., Matalon, M., Peters, N., Sivashinsky, G., and Williams, F. A., "Combustion Theory and Modeling," *Proceedings of the Combustion Institute*, Vol. 30, 2005, pp. 1-19.

[3] Chakravarthi, V. K., and Menon, S., "Large-Eddy Simulation of Turbulent Premixed Flames in the Flamelet Regime," *Combustion Science and Technology*, Vol. 162, 2000, pp. 133-161.

[4] Chen, Y.-C, Peters, N., Schneemann, G. A., Wruck, N., Renz, U., and Mansour, M. S., "The Detailed Flame Structure of Highly Stretched Turbulent Premixed Methane-Air Flames," *Combustion and Flame*, Vol. 107, 1996, pp. 223-244.

[5] Colin, O., Ducros, F., Veynante, D., and Poinsot, T., "" A Thickened Flame Model for Large Eddy Simulation of Turbulent Premixed Combustion," *Physics of Fluids*, Vol. 12, No. 7, 2000, pp. 1843-1863.

[6] Correa, S. M., "Power Generation and Aeropropulsion Gas Turbines: From Combustion Science to Combustion Technology," *Proceedings of the Combustion Institute*, Vol. 27, 1998, pp. 1793-1807.

[7] Duchamp de Lageneste, L., and Pitsch, H., "A Level-Set Approach to Large Eddy Simulation of Premixed Turbulent Combustion,", Center for Turbulence Research, Annual Research Briefs, 2000, pp. 105-116.

[8] Eggenspieler, G., and Menon, S., "Large-Eddy Simulation of Pollutant Emission in a DOE-HAT Combustor," *Journal of Propulsion and Power*, Vol. 20, No. 6, 2004, pp. 1076-1085.

[9] Flohr, P., and Pitsch, H., "A Turbulent Flame Speed Closure Model for LES of Industrial Burner Flows," Center for Turbulence Research, Annual Research Briefs, 2000, pp. 169-179.

[10] Fye, D. J., "Economical Evaluation of Runge-Kutta Formulae," *Mathematics of Computation*, Vol. 20, No. 95, 1966, pp. 392-398.

[11] Gaitonde, D. and Visbal, M., "High-Order Schemes for Navier-Stokes Equations: Algorithm and Implementation into FDL3DI," Technical Report AFRL-VA-WP-TR-1998-3060, Air Force Research Laboratory, Wright-Patterson AFB, 1998.

[12] Germano, M., Piomelli, U., Moin, P., and Cabot, W. H., "A Dynamic Subgrid-Scale Viscosity Model," *Physics of Fluids A,* Vol. 3, No. 7, 1991, pp. 1760-1765.

[13] Harten, A., Engquist, B., Osher, S., and Chakravarthy, S., "Uniformly high order essentially non-oscillatory schemes, III," *Journal of Computational Physics*, Vol. 71, 1987, pp. 231-303.

[14] Huang, Y., "Modeling and Simulation of Combustion Dynamics in Lean-Premixed Swirl-Stabilized Gas-Turbine Engines," Ph.D. Dissertation, Mechanical Engineering, The Pennsylvania State Univ., 2003.

[15] Huang, Y., Sung, H.-G., Hsieh, S.-Y., and Yang, V., "Large-Eddy Simulation of Combustion Dynamics of Lean-Premixed Swirl-Stabilized Combustor," *Journal of Propulsion and Power*, Vol. 19, No. 5, 2003, pp. 782.

[16] Kazakov, A., and Frenklach, M., http://www.me.berkeley.edu/drm [cited December 2, 2005].

[17] Kee, R. J., Grcar, J. F., Smooke, M. D., and Miller, J. A., "A Fortran Program for Modeling Steady Laminar One-Dimensional Premixed Flames," Technical Report SAND85-8240, Sandia National Laboratories, 1985.

[18] Kee, R. J., Rupley, F. M., and Miller, J. A., "CHEMKIN-II: A Fortran Chemical Kinetics Package for the Analysis of Gas-Phase Chemical Kinetics," Technical Report SAND89-8009, Sandia National Laboratories, 1989.

[19] Kim, W. W., Menon, S., and Mongia, H. C., "Large Eddy Simulation of a Gas Turbine Combustor Flow," *Combustion Science and Technology*, Vol. 143, 1999, pp. 25-62.

[20] Lele, S. K., "Compact Finite Differences with Spectral-Like Resolution," *Journal of Computational Physics,* Vol. 103, No. 1, 1992, pp. 16-42.

[21] Lilly, D.K., "A Proposed Modification of the Germano Subgrid-Scale Closure Model," *Physics of Fluids A,* Vol. 4, 1992, pp. 633.

[22] Lipatnikov, A. N., and Chomiak, J., "Turbulent Flame Speed and Thickness: Phenomenology, Evaluation, and Application in Multi-Dimensional Simulations," *Progress in Energy and Combustion Science*, Vol. 28, No. 1, 2002, pp. 1-74.

[23] Lutz, A. E., Kee, R. J., Grcar, J. F., and Rupley, F. M., "OPPDIF: A Fortran Program for Computing Opposed-Flow Diffusion Flames," Technical Report SAND96-8243, Sandia National Laboratories, 1996.

[24] Menon, S., and Jou, W. H., "Large-Eddy Simulation of Combustion Instability in an Axisymmetric Ramjet Combustor," *Combustion Science and Technology*, Vol. 75, 1991, pp. 53-72.

[25] Moin, P., Squires, K., Cabot, W. H., and Lee, S., "A Dynamic Subgrid-Scale Model for Compressible Turbulence and Scalar Transport," *Physics of Fluids A,* Vol. 3, No. 11, 1991, pp. 2746-2757.

[26] Nilsson, P., and Bai, X. S., "Level-Set Flamelet Library Approach for Premixed Turbulent Combustion," *Experimental Thermal and Fluid Science,* Vol. 21, 2000, pp. 87-98.

[27] Nilsson, P., and Bai, X. S., "Effects of Flame Stretch and Wrinkling on CO Formation in Turbulent Premixed Combustion" *Proceedings of the Combustion Institute*, Vol. 29, 2002, pp.1873-1879.

[28] Peters, N., *Turbulent Combustion*, Cambridge University Press, 2000.

[29] Pitsch, H. and Duchamp de Lageneste, L., "Large-Eddy Simulation of Premixed Turbulent Combustion Using a Level-Set Approach," *Proceedings of the Combustion Institute,* Vol. 29, 2002, pp. 2001-2008.

[30] Russo, G., and Smereka, P., "A Remark on Computing Distance Functions," *Journal of Computational Physics*, Vol. 163, 2000, pp. 51-67.

[31] Shu, C.-W., "Efficient Implementation of Essentially Non-Oscillatory Shock Capturing Schemes," *Journal of Computational Physics*, Vol. 77, 1988, pp. 439-471.

[32] Shu, C.-W., "Efficient Implementation of Essentially Non-Oscillatory Shock Capturing Schemes, II," *Journal of Computational Physics*, Vol. 83, 1989, pp. 32-78.

[33] Shu, C.-W., "Essentially Non-Oscillatory and Weighted Essentially Non-Oscillatory Schemes for Hyperbolic Conservation Laws," ICASE Report No. 97-65, November 1997.

[34] Smith, G. P., Golden, D. M., Frenklach, M., Moriarty, N. W., Eiteneer, B., Goldberg, M., Bowman, C. T., Hanson, R. K., Song, S., Gardiner, W. C., Lissianski, V. V., and Qin, Z., http://www.me.berkeley.edu/gri_mech [cited December 2, 2005].

[35] Smagorinsky, J., "General Circulation Experiments with the Primitive Equations. I. The Basic Experiment," *Monthly Weather Review,* Vol. 91, No. 3, 1963, pp. 99.

[36] Sussman, M., and Fatemi, E., “An Efficient, Interface-Preserving Level Set Redistancing Algorithm and its Application to Interfacial Incompressible Fluid Flow,” *SIAM Journal on Scientific Computing*, Vol. 20, No. 4, 1999, pp. 1165-1191.
[37] Sussman, M., Smereka, P., and Osher, S., “A Level Set Approach for Computing Solutions to Incompressible Two-Phase Flows,” *Journal of Computational Physics*, Vol. 119, 1994, pp. 146-159.
[38] Thibaut, D., and Candel, S., “Numerical Study of Unsteady Turbulent Premixed Combustion: Application to Flashback Simulation,” *Combustion and Flame*, Vol. 113, 1998, pp. 53-65.
[39] Visbal, M., and Gaitonde, D., “On the Use of Higher-Order Finite-Difference Schemes on Curvilinear and Deforming Meshes,” *Journal of Computational Physics*, Vol. 181, 2002, pp. 155.
[40] Williams, F. A., “Turbulent Combustion,” *The Mathematics of Combustion*, edited by J. Buckmaster, 1985, pp. 97-131.
[41] Younger G., Gabriel, D., and Mickelsen, W., “Experimental Study of Isothermal Wake-Flow Characteristics of Various Flame Holder Shapes,” NACA RM E51K07, 1951.